AIAA SciTech Forum
January 3-7, 2022, San Diego, CA & Virtual
AIAA SCITECH 2022 Forum

10.2514/6.2022-1983

Evaluating Dynamic Stall Onset Criteria for Mixed and Trailing-Edge Stall

Sarasija Sudharsan *[1], Shreyas Narsipur†[2], and Anupam Sharma‡[1]
[1]*Iowa State University, Ames, IA, 50011*
[2]*Mississippi State University, Mississippi State, MS, 39762*

Our objective is to evaluate two stall onset criteria that are calculated based on flow quantities at the leading-edge, for mixed and trailing-edge stall. The two parameters, namely, the Leading Edge Suction Parameter ($LESP$) [1, 2] and the Boundary Enstrophy Flux (BEF) [3], signal stall onset by reaching their maximum magnitudes before dynamic stall vortex (DSV) formation for leading-edge stall for $Re_c \geq O(10^4)$. However, for mixed and trailing edge stall, leading-edge suction tends to persist even after there is a significant region of reversed flow on the aft portion of the airfoil and stall is underway. This poses a challenge for stall onset criteria focused on the leading-edge, since stall onset might not be indicated at the leading-edge until after it is in progress. We therefore evaluate these parameters for cases with significant trailing-edge separation. Our results are based on numerical simulations using wall-resolved large eddy simulations and unsteady Reynolds-Averaged Navier-Stokes Equations. Our datasets include one clear leading-edge stall and three mixed/trailing-edge stall cases at chord-based Reynolds numbers of 2×10^5 and 3×10^6, respectively. We find that the $LESP$ and $|BEF|$ criteria reach their maxima in advance of DSV formation and lift stall for the leading-edge stall case as well as two of the three cases with significant trailing-edge separation. However, for the extreme trailing-edge case considered, lift stall occurs before either criterion reaches its maximum. The observed trend, based on the four cases, is a decrease in the delay between the parameters reaching their maxima and the crucial point for stall control (DSV formation or lift stall), as trailing-edge separation becomes more significant.

I. Introduction

Dynamic stall is a topic of great interest in unsteady aerodynamics due to its severity compared to static stall [4]. It can occur over aerodynamic surfaces undergoing large amplitude transient motion or unsteady maneuvers, for example, over wind turbine or helicopter rotor blades. The large unsteady aerodynamic loads that are incurred due to dynamic stall can lead to structural damage or failure. This has led to several studies on flow control using leading-edge blowing[5, 6], use of plasma actuation [7, 8], synthetic jets [9], etc. However, the timely application of these control efforts is important, as they are most effective before the formation of the dynamic stall vortex (DSV) [10], a coherent vortex structure that is a characteristic feature of "deep" stalls [4]. Characterizing stall onset is of crucial importance for these control efforts to be deployed in a timely manner.

Various criteria for dynamic stall onset based on the unsteady aerodynamic coefficients have been explored to formulate first-order, semi-empirical, dynamic stall models [11]. However, our interest is in narrowing down the identification of the stall onset point to a finer scale, based on high-fidelity numerical simulations. Currently, the Leading Edge Suction Parameter ($LESP$), a measure of the chord-wise suction force near the leading-edge [1], is widely used for identifying dynamic stall onset [12, 13]. It was used in a low order model to trigger leading-edge vortex shedding when a predetermined (from CFD) critical value was reached. We have used the maximum $LESP$ as a proxy for the critical $LESP$, since max($LESP$) is a standalone criterion that can be evaluated without *a priori* knowledge of the critical $LESP$ value. The calculation of $LESP$ from CFD has been updated [2] to be a scaled force in the camber direction, with a dynamic pressure scaling based on the relative velocity of the airfoil. We recently proposed [3] a vorticity-based criterion, namely, the boundary enstrophy flux (BEF), that reaches its maximum magnitude earlier than the $LESP$, based on wall-resolved large eddy simulations (LES). The scope of that work was limited to leading-edge dynamic stall in incompressible flows.

*Graduate student, Department of Aerospace Engineering, Iowa State University.
†Assistant Professor, Department of Aerospace Engineering, Mississippi State University, Senior Member AIAA.
‡Associate Professor, Department of Aerospace Engineering, Iowa State University, Associate Fellow AIAA.

In the current paper, we extend our work to mixed and trailing-edge stalls in incompressible flows. In a classic leading-edge stall, the collapse in leading-edge suction is accompanied by the bursting of the laminar separation bubble (LSB), with the formation of a DSV close to the leading-edge, with little or no trailing-edge separation. However, a trailing-edge stall [14] occurs due to instabilities arising in the reversed flow moving upstream from the trailing edge. Leading-edge suction persists even after a large region of reverse flow has formed downstream. DSV formation occurs when the trailing-edge reverse flow reaches the leading-edge. This is a significantly different sequence of events compared to leading-edge stall. Therefore, in a purely trailing-edge stall, there is no distinct *leading-edge* boundary layer separation or vortex formation as a result of it [15]. This poses a challenge for stall onset criteria focused on the leading-edge, since stall onset might not be indicated until the trailing-edge reverse flow reaches the leading-edge, by which time *lift stall* might have occurred. Boundary layer separation can also exhibit characteristics of both leading and trailing-edge stall. In such a "mixed" stall, two distinct boundary layer disturbances occur, both near the leading-edge and the trailing-edge, with their subsequent merging/interaction [15]. This would be reflected in the C_f distribution with negative values over the entire airfoil during the time of their interaction (see C_f contours for case B in Fig. 3b).

Our objective is to evaluate these stall onset criteria, namely $LESP$ and BEF, for mixed and trailing-edge stall. The key point of interest is to ascertain if these two parameters reach their maximum values *before* a DSV roll-up occurs, so that effective control measures can be deployed. As previously mentioned, the dynamics of the vortex are harder to control once it has rolled up. However, for trailing-edge stalls, as observed in one of our cases (case D, III.B.2), lift stall occurs before the trailing-edge reverse flow reaches the leading-edge and subsequent DSV formation. This is due to the prevalence of large adverse pressure gradients downstream. We therefore consider the crucial point for stall control to be either (a) formation of a DSV, or (b) lift stall point, whichever occurs earlier. We identify DSV formation from streamlines, C_p, and C_f distributions over the airfoil surface, and lift stall from the maximum in the coefficient of lift (c_l). The four cases illustrating different types/extents of separation are discussed in section II.A.

II. Methods/Details

Our results are based on two types of numerical simulations: wall-resolved LES and unsteady Reynolds-Averaged Navier-Stokes (uRANS). LES were carried out using the compressible flow solver FDL3DI [16, 17], where the effect of sub-grid scale stresses is modeled implicitly by spatial filtering at each timestep, to remove energy at unresolved scales. Spatial discretization uses a sixth-order compact difference scheme, while time integration is carried out using an implicit, approximate factorization technique. Based on prior grid sensitivity studies, we used a grid having 410, 1341 and 134 grid points respectively in the radial, circumferential and spanwise directions. The chosen mesh is highly refined over the suction surface to capture small-scale viscous flow features. We simulated ten percent of airfoil chord in the span-wise direction, with periodic boundary conditions applied at the ends. A statistically stationary solution was first obtained for a static simulation with α fixed at 4°. C_p and C_f distributions over the airfoil were compared with XFOIL and found to be in good agreement. Next, the dynamic pitching motion was simulated through grid motion, with a ramp function that smoothly transitions to the required pitch rate. The results presented are based on 2D flow fields obtained by span-averaging the 3D solution. Further details on the solver, grid, and verification of results are discussed in detail in Sharma and Visbal [16].

The uRANS simulations were performed using the REACTMB-INS code, which solves the time-dependent incompressible Navier-Stokes equations using a finite-volume method. The governing equations are written in arbitrary Lagrangian / Eulerian (ALE) form, which enables the motion of a body-fitted computational mesh in accord with prescribed rate laws. Spatial discretization of the inviscid fluxes uses a low-diffusion flux-splitting method valid in the incompressible limit [18]. This method is extended to higher-order spatial accuracy using Piecewise Parabolic Method interpolations of the primitive variables $[p, u, v, w]^T$ and transported variable for the S-A model, $\tilde{\nu}$. Viscous terms are discretized using second-order central differences. A dual time-stepping method is used to integrate the equations in time. An artificial compressibility technique, discretized in a fully implicit fashion and solved approximately using ILU decomposition, is used to advance the solution in pseudo-time. Typically, eight sub-iterations per physical time step were needed to reduce the residual errors two orders of magnitude. The Spalart-Allmaras model [19] as implemented by Edwards and Chandra [20], is used for turbulence closure. Two-dimensional body-fitted O-grids for the NACA0012 and NACA0018 airfoils containing 140,400 and 149,100 cells, respectively, were generated for the uRANS simulations work. A grid sensitivity study, carried out to ensure grid convergence, showed that decreasing the wall y^+ to a tenth of that used in the final grids does not alter the results noticeably. The current uRANS methodology has been validated against data from wind- and water-tunnel experiments for various unsteady airfoil motions in Refs. [1, 21, 22].

Case	Airfoil	Re_c	Simulation type	Kinematics	Stall type
A	NACA0012	2×10^5	LES/RANS	Constant pitch-up, $K = 0.025$	Leading-edge
B	NACA0018	2×10^5	LES	Constant pitch-up, $K = 0.025$	Mixed
C	NACA0012	3×10^6	RANS	Sinusoidal, $\alpha_{max} = 45°$, $K = 0.075$	Mixed / Trailing-edge
D	NACA0012	3×10^6	RANS	Sinusoidal, $\alpha_{max} = 35°$, $K = 0.005$	Trailing-edge

Table 1 Datasets used in present work.

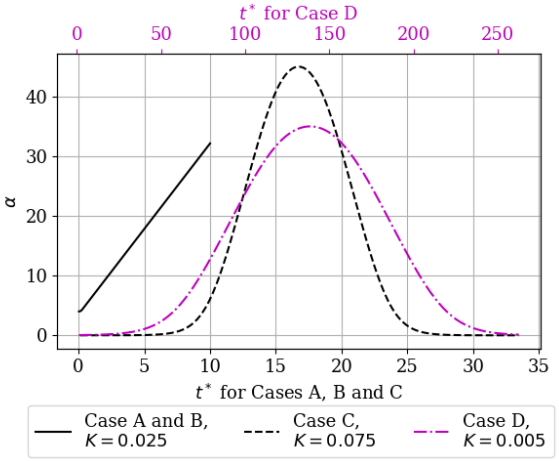

Fig. 1 α vs t^* for the four cases presented.

A. Datasets used

Details on the four cases discussed in the current paper (airfoil geometries, Re_c, kinematics, etc.) are listed in Table 1. One leading-edge stall case (case A) is presented to distinguish its flow characteristics from mixed/ trailing-edge stall. We simulated airfoils undergoing either a constant-rate pitch-up (cases A and B) or a pitch-up-return type generated from Eldredge's formulation (cases C and D; see [2] for details), pivoted about the quarter-chord point. Figure 1 compares the kinematics of the four cases. The variation in α is plotted with non-dimensional time, $t^*(= tU_\infty/c)$, for each case. The non-dimensional pitch rate, K, which is defined as the maximum value of $(1/2)d\alpha_{rad}/dt^*$ for each case, (where α_{rad} is α in radians), represents the level of unsteadiness or phase lag between the pitching and fluid motion [14]. Cases A, B and C have a moderately high value of K, while case D has a very low value. Note that t^* for Case D has been plotted on a separate axis (in pink) since it has a very low pitch rate. The Re_c used were moderately high to high since our interest is in capturing mixed/trailing-edge stall. $Ma = 0.1$ for all cases.

B. $LESP$ and BEF definitions

The objective of the current work is to evaluate the $LESP$ and BEF criteria for stall onset for mixed and trailing-edge stalls.

The $LESP$, which is a measure of the suction at the leading edge, is calculated from CFD/experimental results by determining the suction force using surface pressure measurements [2]. The approach is rooted in the fact that, when the stagnation point is not at the geometric leading edge of the airfoil, the flow is forced to travel around the rounded leading edge. This flow curvature gives rise to a low-pressure region near the leading edge. The net force acting on the leading edge is resolved into components acting along and normal to the direction of the camber line at the leading edge. The component of force along the camber line is often a "suction" force acting in the forward direction. The leading-edge force on the airfoil, obtained by integrating the surface pressure on the forward portion of the airfoil from the leading edge to the x/c for the maximum-thickness location (denoted by $(x/c)_{max}$), is then split into its suction and normal components which, when non-dimensionalized by the net dynamic pressure ($q_\infty = \rho U_\infty^2/2$, where ρ is the freestream density) and chord, give the coefficients of suction, $C^{\text{ref}}_{s,LE}$, and normal force, $C^{\text{ref}}_{n,LE}$, on the leading edge.

Fig. 2 Schematic showing limits of integration for calculating BEF and $LESP$. x/c for BEF is set to $0.01c$ based on prior results [3]; x/c for $LESP$ is set to location of maximum airfoil thickness [2].

$$C^{\text{ref}}_{s,LE} = F_{S,LE}/q_\infty c \tag{1}$$

$$C^{\text{ref}}_{n,LE} = F_{N,LE}/q_\infty c \tag{2}$$

As shown by Ramesh et. al [23], airfoil theory gives the relationship between $C^{\text{ref}}_{s,LE}$ and $LESP$ as

$$C^{\text{ref}}_{s,LE} = 2\pi(LESP)^2 \tag{3}$$

The sign of the $LESP$ is set to be the same as that of the $C^{\text{ref}}_{n,LE}$, so that positive $C^{\text{ref}}_{n,LE}$ is assumed to correspond to a flow with stagnation point on the lower surface, and vice versa. Additionally, to ensure compatibility with theory, the CFD/experiment-derived $LESP$ is set to zero at the few time instants when the $C^{\text{ref}}_{s,LE}$ has a negative value. Thus, the $LESP$ is calculated from $C^{\text{ref}}_{s,LE}$ and $C^{\text{ref}}_{n,LE}$ as:

$$LESP = \begin{cases} \text{sgn}(C^{\text{ref}}_{n,LE})\sqrt{\frac{C^{\text{ref}}_{s,LE}}{2\pi}}, & \text{for} \quad C^{\text{ref}}_{s,LE} > 0 \\ 0, & \text{for} \quad C^{\text{ref}}_{s,LE} \leqslant 0 \end{cases} \tag{4}$$

Next, we define the other criterion under consideration, namely, the boundary enstrophy flux. Enstrophy is the square of vorticity magnitude $|\boldsymbol{\omega}|^2$. This simplifies to ω^2, the square of the spanwise vorticity for our 2D flow fields. We consider the integral of its flux from the wall, i.e., $\partial(\omega^2/2)/\partial n = \omega(\partial\omega/\partial n)$. The integrated boundary enstrophy flux (BEF) is defined in Equation (5). It is divided by Re_c so that it can be viewed as a product of vorticity (ω) and boundary vorticity flux defined as $(1/Re_c)\partial\omega/\partial n$. The integral is carried out between x/c on the pressure side to x/c on the suction side, as shown in Fig. 2.

$$BEF = \frac{1}{Re_c}\int_{(x/c)_p}^{(x/c)_s} \omega\frac{\partial\omega}{\partial n}ds \tag{5}$$

The BEF can be thought of as an integral of the product of the vorticity and streamwise pressure gradient, due to the proportional growth of the vorticity flux and streamwise pressure gradient at the wall. That is, $(1/Re_c)\partial\omega/\partial n \sim (1/\rho)\partial p/\partial s$, for small tangential surface acceleration. Therefore, large contributions to the BEF arise only from regions of high vorticity combined with large pressure gradients. Based on recent work on leading-edge dynamic stall onset [3], we found that the most dominant contribution arises from the laminar leading-edge region, where there is large favorable pressure gradient / clockwise vorticity, as flow accelerates around the leading-edge. As this region is very small, the integral for BEF is carried out over 1% chord (that is, from $0.01c$ on the pressure side to $0.01c$ on the suction side). When the favorable pressure gradient drops with the LSB burst, the BEF magnitude also drops, after reaching a maximum. Since the bursting of the LSB occurs before DSV formation, the BEF reaches its maximum magnitude before the roll-up of the DSV. Further, we find that the BEF reaches its maximum before the $LESP$ in such leading-edge stalls. However, in trailing-edge stalls, leading-edge suction tends to persist for longer [24], even with the prevalence of large regions of reverse flow downstream. It is therefore expected that the peak value of the BEF would occur later as well.

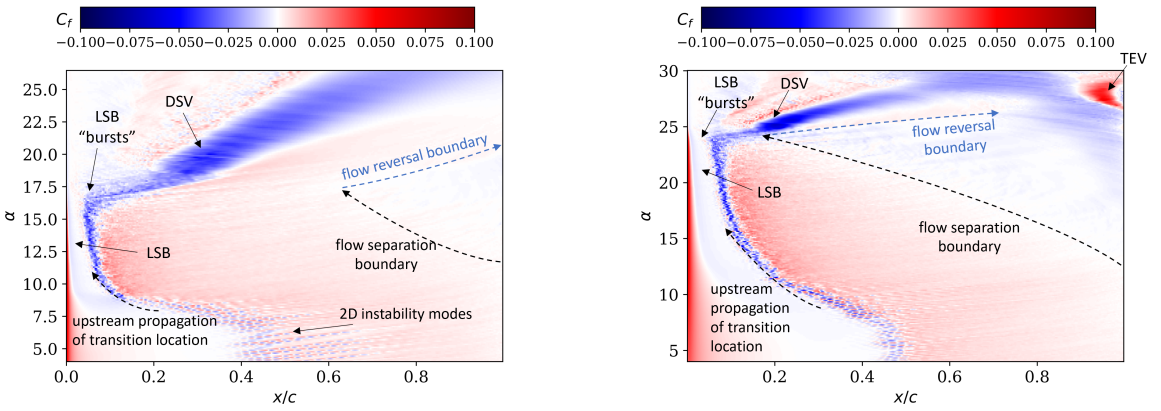

(a) x-t diagram for NACA 0012 (case A)

(b) x-t diagram for NACA 0018 (case B)

Fig. 3 Space-time diagrams of friction coefficient, C_f, on the suction surface of (a) NACA0012 and (b) NACA0018, both at $Re_c = 200,000$ and undergoing a constant-rate pitch-up maneuver. The flow reversal originating from the trailing edge is much more significant in the mixed type stall in (b) compared to the leading edge type stall in (a).

III. Results and Discussion

A. Comparison between leading-edge and mixed stall from LES results (cases A and B)

Space-time contours of the friction coefficient C_f on the suction surface of the airfoil are used to elucidate the sequence of flow events that occur as the unsteady motion progresses. Fig. 3a shows the space-time diagram on the suction surface for the NACA0012 airfoil undergoing a constant-rate pitch-up motion at $Re_c = 200,000$. This corresponds to Case A in Table 1. The x-axis represents the chord-wise distance on the suction surface and the y-axis, the angle of attack, with relevant flow events marked in the figure. As the airfoil pitches up, the transition point moves upstream, with the eventual formation of an LSB due to laminar separation and turbulent reattachment of the boundary layer [25]. As α increases, at certain point, the LSB fails to reattach due to the insurmountably large adverse pressure gradient downstream of the suction peak, and breaks down or "bursts". After the bursting of the LSB, flow characteristics are dominated by the DSV, whose imprint (in blue) is seen convecting downstream. While some flow reversal is seen at the trailing edge, it is insignificant.

On the contrary, in a mixed stall, as shown for the NACA0018 airfoil for the same maneuver and Re_c (Case B) in Fig. 3b, this flow reversal is predominant and interacts with the leading edge. There is boundary layer breakdown at the leading-edge from the bursting of the LSB, as well as upstream propagation of trailing-edge separated flow, with their subsequent merging. Around 23°, when these flows interact, there is negative C_f over the entire airfoil suction surface (compare with C_f contours for NACA0012 in Fig. 3a , where this never happens). This behavior agrees with the definition of "mixed" stall[15] we have used. The DSV is seen convecting downstream after the interaction between leading and trailing-edge separated flows. The larger thickness of the NACA0018 airfoil has the effect of postponing the point of stall onset along the time axis, since the adverse pressure gradient following the suction peak at the leading-edge is lower. Figure 4 shows C_p profiles at a few α for the two cases, contrasting the flow features between leading-edge and mixed stalls. Note that a large region of trailing-edge reverse flow is present before the collapse of leading-edge suction for the NACA0018 airfoil or case B. For a purely trailing-edge stall, the reverse flow region propagating upstream from the trailing-edge tends to dominate flow dynamics. The DSV could either be a strong leading-edge vortex from leading-edge separation, or trailing-edge reverse flow that grows into a dominant coherent structure. In general, trailing-edge type stalls are expected for thicker airfoils and/or higher Re_c. Due to the large computational expense of LES simulations, particularly at higher Re_c we have used RANS simulations for these cases. See the appendix for a comparison of results between LES and RANS for case A, demonstrating that they match closely.

The higher Re_c cases (cases C and D) carried out using RANS will be discussed in detail next.

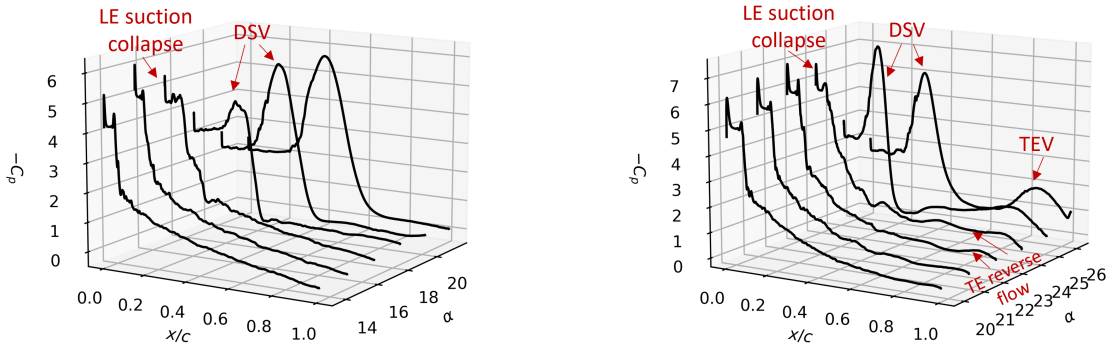

(a) NACA 0012 (case A) **(b) NACA 0018 (case B)**

Fig. 4 C_p profiles on the suction side at a few α showing features of leading-edge (a) and mixed (b) stall.

B. RANS results for higher Re_c cases

1. Case C: NACA0012, $Re_c = 3 \times 10^6, K = 0.075$

Case C corresponds to the NACA0012 airfoil undergoing a sinusoidal pitching motion, pivoted about the quarter-chord point at a non-dimensional pitch rate of 0.075. The Re_c is 3×10^6 and $Ma = 0.1$.

Fig. 5 shows the variation of the unsteady aerodynamic coefficients with t^*. The three panels show respectively the coefficient of lift (c_l), drag (c_d), and moment (c_m). The variation of α with time is also plotted in blue in the top panel for reference. We observe three instances between t^* of 13 and 20, where c_m sharply diverges, indicating moment stall. Lift stall follows the first moment stall, around $t^* = 14.7$. Leading-edge suction collapses around $t^* = 14.3$ (Fig. 8); this is discussed further in the following paragraph.

As the airfoil pitches up, reverse flow from the trailing edge moves upstream as shown in the C_f space-time contours in Fig. 6b. The reverse flow interacts with the leading-edge flow, resulting in the formation of a strong DSV around the quarter-chord point, which is pointed out in the C_f space-time contours shown in Fig. 6b. It is hard to determine if the trailing-edge reverse flow has reached all the way up to the leading-edge before DSV formation, so we have classified this case as being in between mixed and trailing-edge stall. The redistribution of lift to be more dominant in the aft portion of the airfoil as the DSV center moves downstream causes a large pitch-down moment, which is the first moment stall point seen in the bottom panel of Fig. 5. The DSV also contributes to increased lift over the airfoil surface as seen from the top panel of Fig. 5. A lift stall results when the DSV convects downstream and away from the airfoil surface. Its imprint (in yellow) can be seen moving downstream in the C_p contours. A zoomed-in view of the space-time contours of $-C_p$ and C_f around the lift stall point are provided in Fig. 7a and 7b. The C_f contours show the upstream propagation of trailing-edge reverse flow. The downstream propagation of the DSV is clearly seen from the C_p contours. Though the influence of the DSV grows weaker, by $t^* = 16.8$ or $\alpha = 45°$, it extends over nearly the entire airfoil suction surface. The presence of the DSV close to the wall [26] induces a counter-clockwise (CCW), trailing-edge vortex (TEV). Though the low pressure region of the TEV contributes to only a small increase in lift, it induces a large pitch-down moment due to the longer moment arm (trailing-edge to quarter-chord point). This explains the second moment stall in 5. By this point, the angle of attack has begun to decrease and the TEV is also shed. An induced clockwise (CW) vortex develops as shown in Fig. 6b as the TEV sheds, contributing a further increase in lift. The formation and propagation of this vortex downstream explains the third moment stall. Around $t^* = 20.6$, with decreasing α, this vortex detaches from the leading-edge and moves away from the airfoil surface. The events described are shown as a sequence in Fig. 9.

Fig. 8 shows the variation of maximum magnitude of C_p near the leading-edge (upto 5 % chord on the suction surface) with t^* in black. α is shown in blue. Leading-edge suction drops sharply around the $t^* \sim 14.3$ or $\alpha \sim 35°$. This is shortly followed by DSV formation at $t^* \sim 14.5$ and lift stall at $t^* \sim 14.7$.

2. Case D: NACA0012, $Re_c = 3 \times 10^6, K = 0.005$

Case D has a much lower non-dimensional pitch rate of $K = 0.005$ compared to Case C ($K = 0.075$). α_{max} is set to 35°. Due to the slower motion, the range of t^* for this case is much larger compared to Case C.

The variation of unsteady aerodynamic coefficients with t^* is plotted is Fig. 10. The top panel shows the variation in

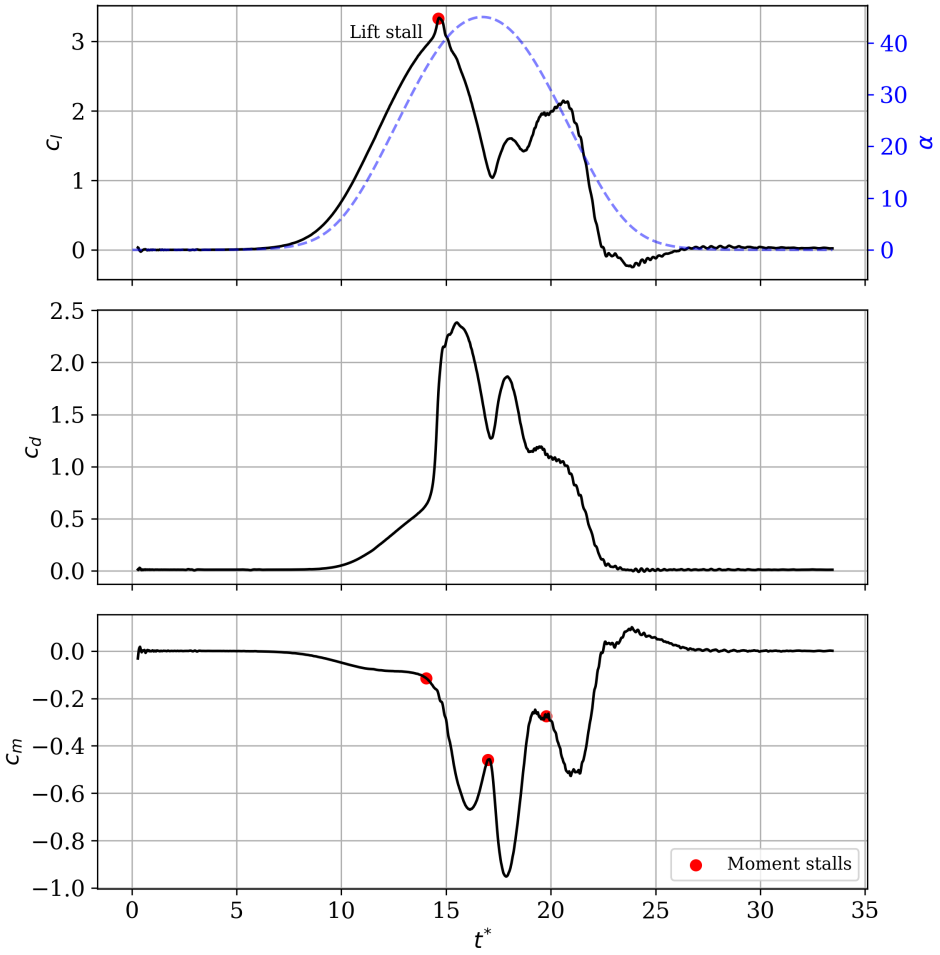

Fig. 5 Unsteady aerodynamic coefficients for Case C.

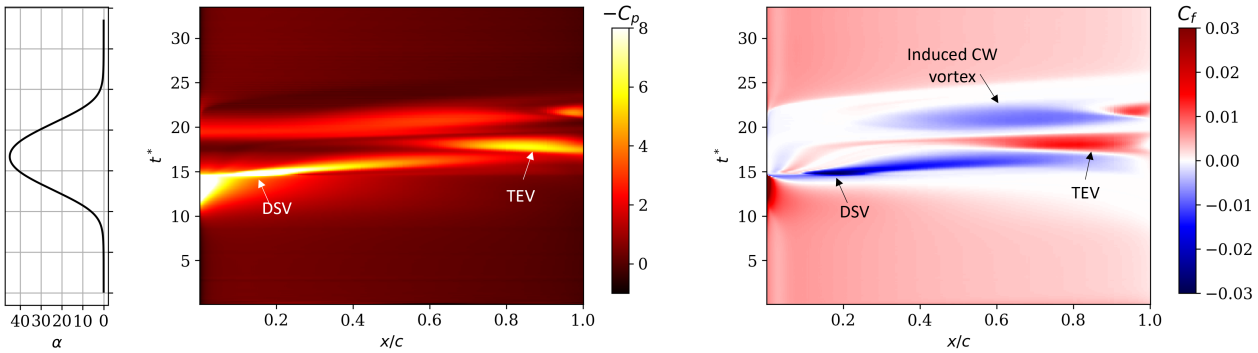

(a) $-C_p$ **(b)** C_f

Fig. 6 Space-time contours of $-C_p$ **(a) and** C_f **(b) for Case C.**

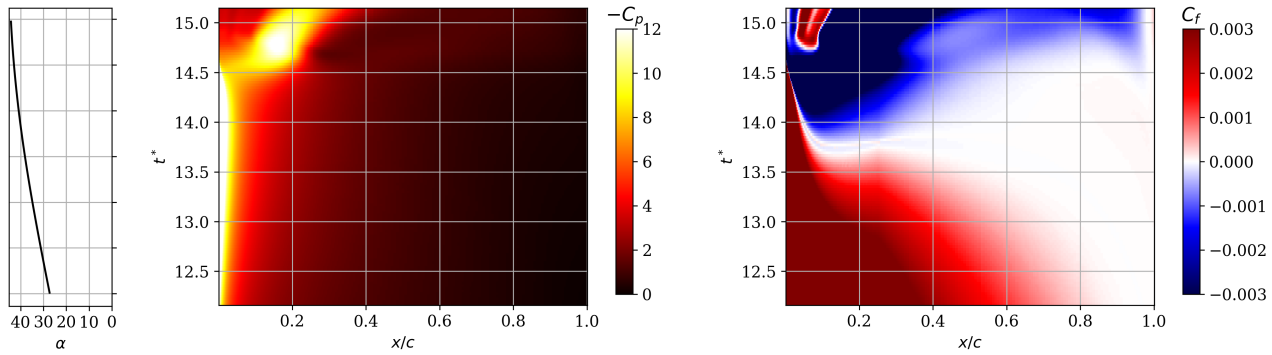

(a) $-C_p$ **(b)** C_f

Fig. 7 Space-time contours of $-C_p$ (a) and C_f (b) for Case C, zoomed in around the lift stall point.

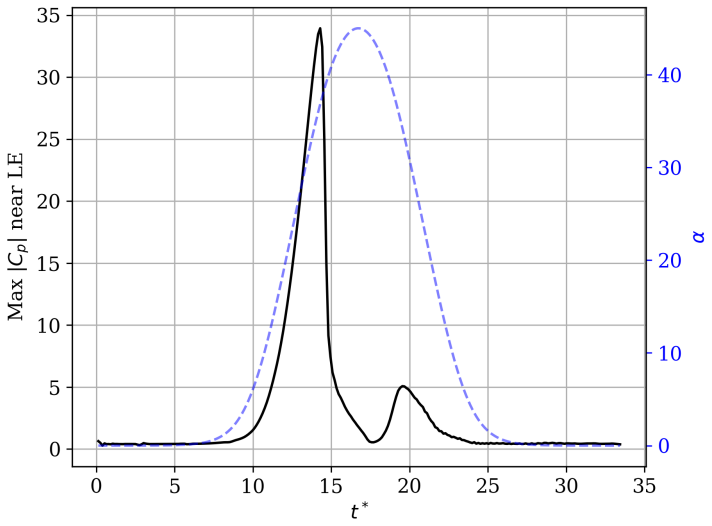

Fig. 8 Variation of max. $|C_p|$ near the leading-edge (up to 5% chord) with t^* for Case C. Variation of α shown in blue. Leading-edge suction collapses around $t^* = 14.3$ or $\alpha = 35°$.

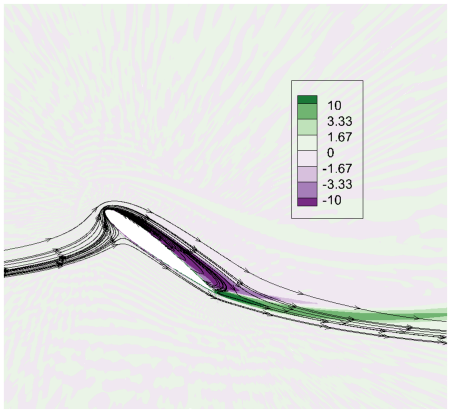

(a) $t^* = 14.3, \alpha = 36.8° \uparrow$

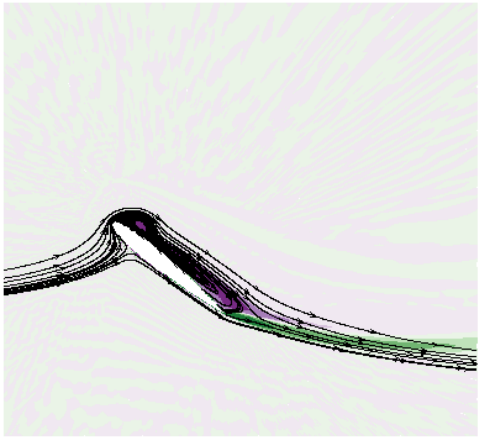

(b) $t^* = 14.7, \alpha = 39.8° \uparrow$

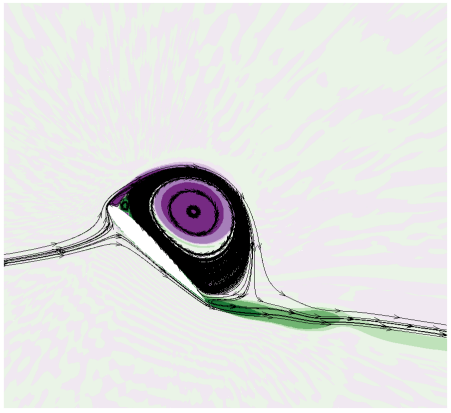

(c) $t^* = 16.0, \alpha = 44.3° \uparrow$

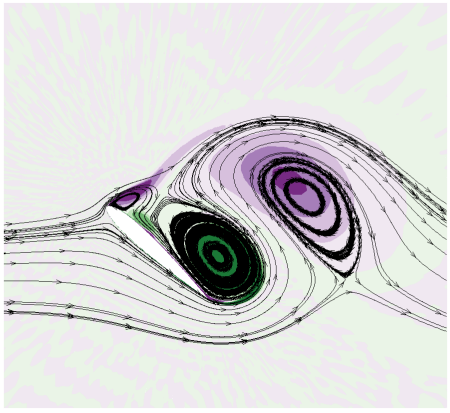

(d) $t^* = 18.1, \alpha = 42.4° \downarrow$

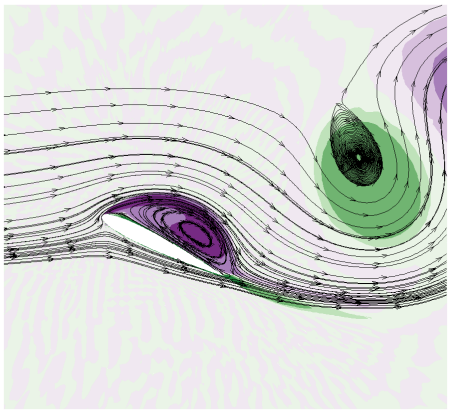

(e) $t^* = 20.6, \alpha = 26.2° \downarrow$

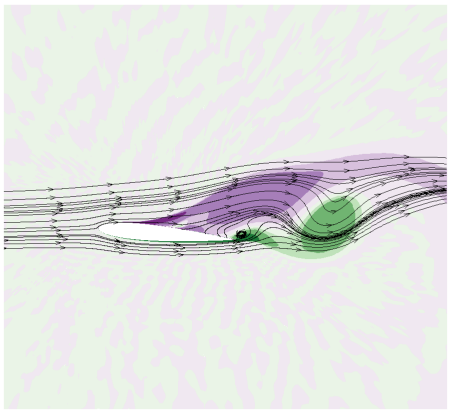

(f) $t^* = 23.7, \alpha = 4.9° \downarrow$

Fig. 9 Streamlines overlaid with vorticity contours for Case C (direction of arrows in the subfigure captions refers to the pitch-up (↑) or pitch-down (↓) part of the motion; contour legend is shown in subfigure (a)).

coefficient of lift, c_l. The variation in α is shown in blue for reference. Lift stall occurs around $t^* = 96.1$ or $\alpha = 21.8°$. Moment stall precedes lift stall very closely, as observed from the bottom panel of Fig. 10. In the present case, stall occurs before DSV formation, due to the loss of circulation from the large region of reverse flow over most of the airfoil. Following this, there is a period of weak vortex shedding with change in α. This is due to the very low pitch-rate for this case, comparable to quasi-steady variation in α. The lift distribution recovers around $t^* = 180$ when α is low enough for the flow to reattach over the airfoil surface. This also induces a slight pitch-up moment observed from the c_m plot.

Space-time contours of C_p and C_f are shown in Fig. 11a and 11b respectively. Reverse flow from the trailing-edge moves upstream beginning at around $t^* = 77$. At this low pitch rate, no leading-edge vortex is formed. As the reverse flow moves upstream and reaches the leading-edge, the adverse pressure gradient over the aft portion of the airfoil becomes increasingly large, leading to lift stall, and subsequently, a collapse in leading-edge suction. Streamlines close to the lift stall point are shown in Fig. 14 (a). There is a small region of recirculating flow from about mid-chord to the trailing-edge when lift stall occurs. The drop in leading-edge suction occurs around $t^* \sim 98$, after lift stall at $t^* \sim 96.1$. The collapse in leading-edge suction can also be observed from Fig. 13, which shows the variation of maximum C_p magnitude near the leading-edge. This case illustrates the persistence of the leading-edge suction peak even after lift stall is underway, when there is significant trailing-edge separation.

A weak DSV is formed from the trailing-edge reverse flow. This is marked in Fig. 11b. Figs. 12a and 12b provide a zoomed-in view of the region around lift stall and DSV formation. We take the point of DSV formation to be around $t^* = 102.4$, when a recirculating region occupies most of the airfoil surface (note strong negative C_f region in zoomed view). This is a rough estimate; it is the lift stall point that we will consider to be the critical point for stall control, since it occurs earlier. Following this, there is a period of weak vortex shedding between $t^* = 105$ and $t^* = 175$ where the lift over the airfoil remains low. As α reduces below 25° ($t^* > 175$) during the pitch down part of the motion, leading-edge suction recovers (seen from the C_p contours in Fig. 11a and Fig. 13). The leading-edge suction drops again due to the continued reduction in α. Fig. 14 shows streamlines overlaid with vorticity contours illustrating the events described above.

C. $LESP$ and BEF criteria for trailing-edge stall

The objective of this paper is to evaluate the $LESP$ and BEF criteria for mixed and trailing-edge type stalls. Both these parameters are calculated based on flow quantities at the leading-edge. As previously explained, leading-edge suction tends to persist for longer in trailing-edge stalls, even after stall is underway.

Figure 15 shows the variation in $LESP$ (black) and $|BEF|$ (green) with time for all four cases. The vertical lines signify the location of their maxima. The point of DSV formation (solid, orange) and lift stall (dashed, red) are also marked. As explained in the introduction, we will evaluate the $LESP$ and BEF criteria against whichever point occurs earlier (DSV formation or lift stall) for each case. The top panel within each subfigure shows the variation of α with time. Clearly, both parameters exhibit critical behavior, i.e., reach their maximum magnitudes, in the vicinity of stall onset. For the higher Re_c cases with sinusoidal motion, where leading-edge suction recovers somewhat as α decreases during the pitch-down part of the motion, the $LESP$ reaches a second peak. Since the $LESP$ represents a chord-wise force, leading-edge suction recovery rotates the force vector towards the leading-edge, resulting in an increase in the chord-wise component. The BEF shows a small second peak only for Case D. This simply reflects the much lower magnitude of C_p corresponding to the second peak relative to the first. Ratio of the C_p magnitude of the second peak relative to the first for Case C and Case D (identified from Fig. 8 and Fig. 13) are respectively 0.14 and 0.4. The leading-edge suction magnitude as flow reestablishes during pitch-down is much weaker for Case C compared to Case D. This reflected in both, the favorable pressure gradient, and the clockwise vorticity at the leading-edge, which is captured by the BEF. Therefore, there is a larger disparity in BEF magnitudes between the two peaks.

We next analyze the behavior of both parameters relative to DSV formation/lift stall. A general observation is that as trailing-edge separation becomes more significant, the gap between DSV formation and lift stall narrows considerably. For cases A and B, DSV formation occurs $3\Delta t^*$ and $0.6\Delta t^*$ before their respective lift stalls. For case C, DSV formation occurs just $0.2\Delta t^*$ before lift stall. Still, for cases A, B and C, DSV formation occurs earlier. For case D, lift stall occurs before DSV formation. For Case A, which undergoes a leading-edge stall, both parameters clearly reach their maxima in advance of DSV formation. The BEF reaches its maximum magnitude about 0.8° of rotation before the $LESP$. However, this delay gets narrower for Case B (NACA 0018) which undergoes a mixed type of stall and is nearly zero for cases C and D. For case C, DSV formation occurs at a $\Delta t^* \sim 0.27$ or $\Delta\alpha \sim 1.6°$ after the parameters' maxima is reached. For case D, lift stall occurs earlier than the parameters' maxima by about $\Delta t^* \sim 1.3$ or $\Delta\alpha \sim 0.7°$.

In summary, we find that the $LESP$ and BEF criteria signal leading-edge and two of the three cases with significant

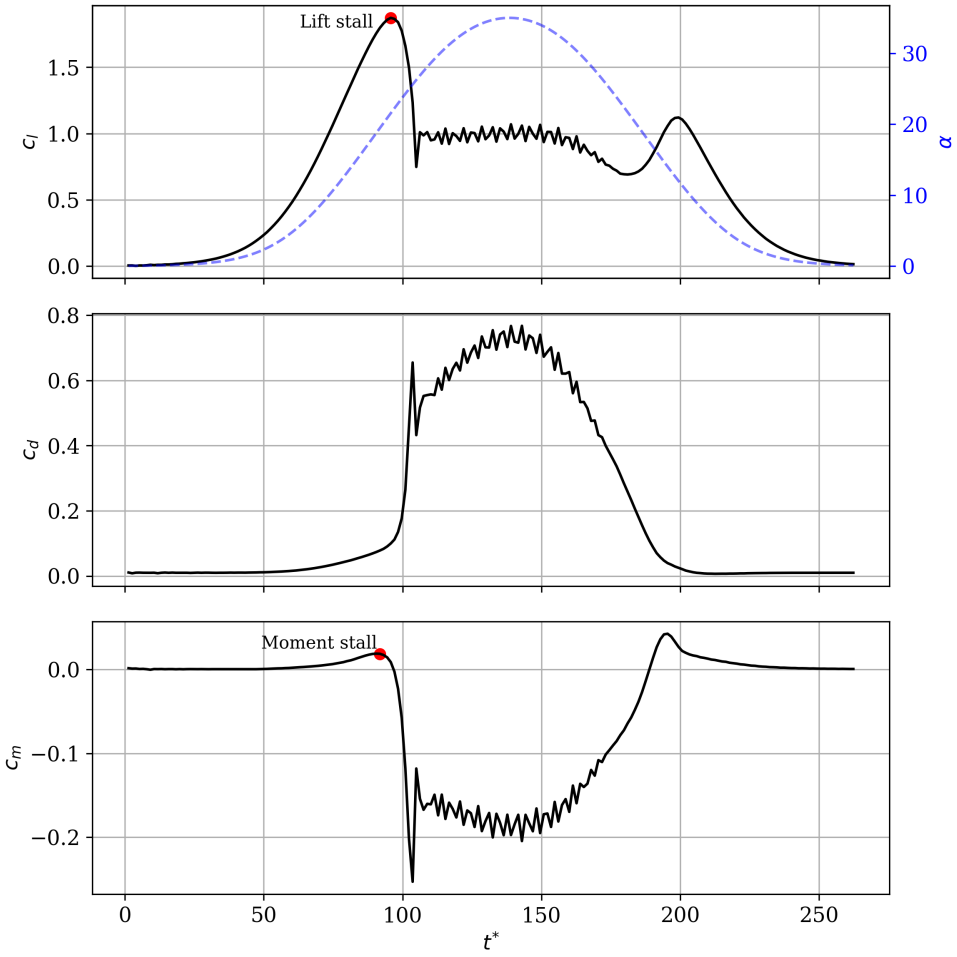

Fig. 10 Unsteady aerodynamic coefficients for Case D.

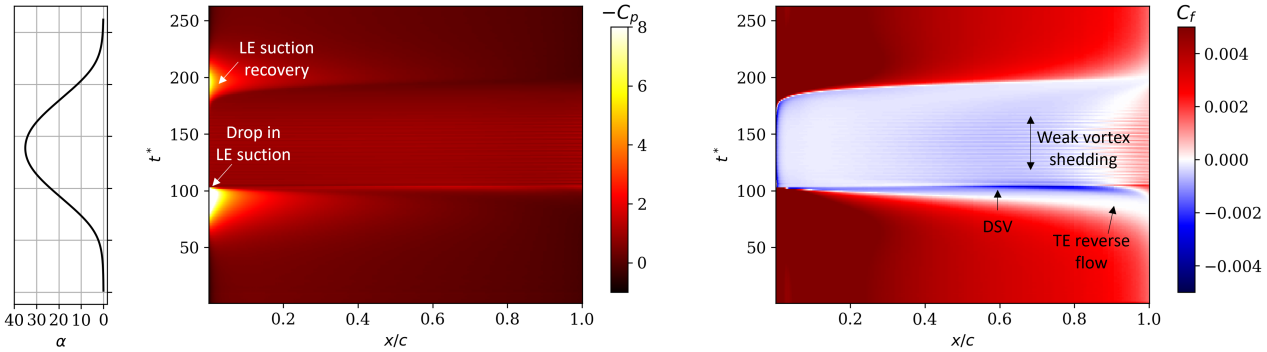

(a) $-C_p$ **(b) C_f**

Fig. 11 Space-time contours of $-C_p$ (a) and C_f (b) for Case D.

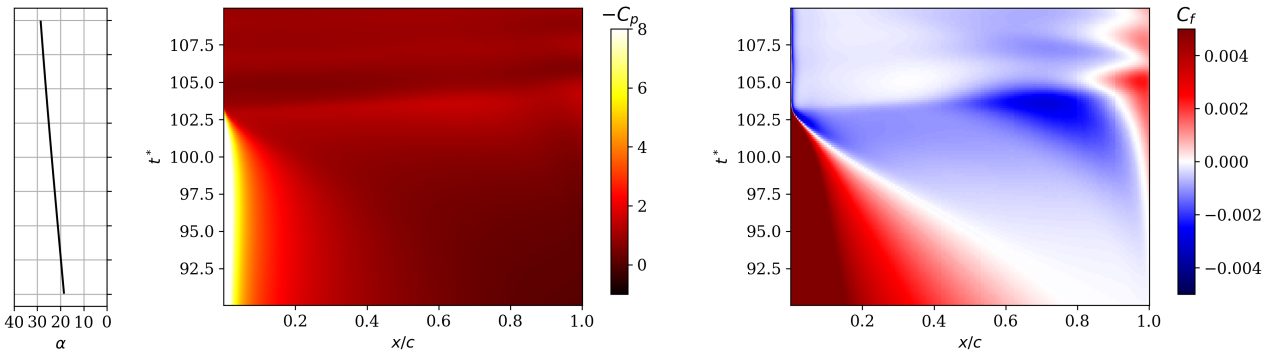

(a) $-C_p$ **(b)** C_f

Fig. 12 Space-time contours of $-C_p$ (a) and C_f (b) for Case D, zoomed in around the lift stall point

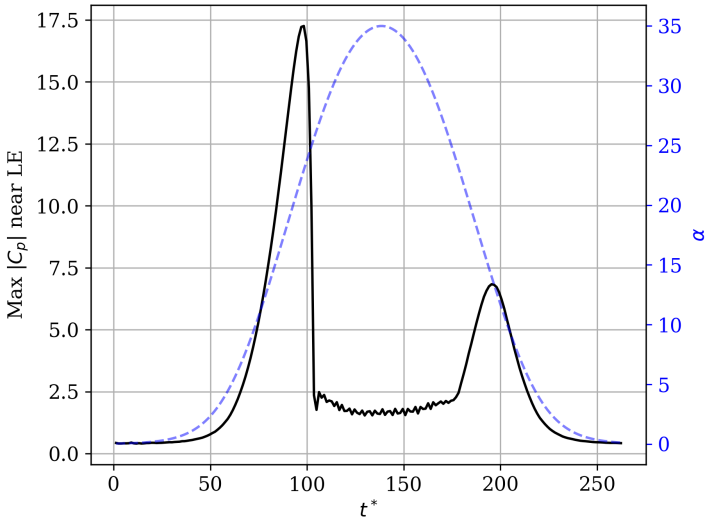

Fig. 13 Variation of max. $|C_p|$ near the leading-edge (up to 5% chord) with t^* for Case D. Variation of α shown in blue. Leading-edge suction collapses around $t^* = 97.8$ or $\alpha = 22.7°$.

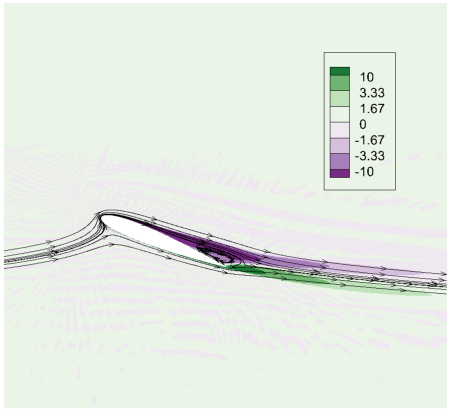

(a) $t^* = 96.1, \alpha = 21.8° \uparrow$

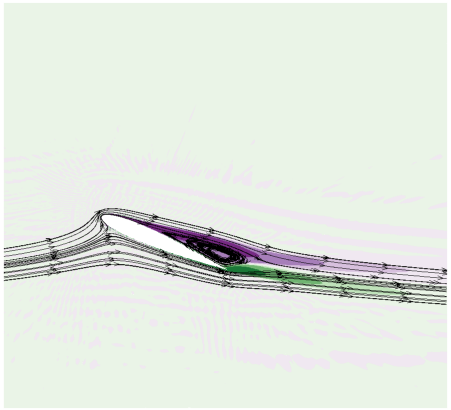

(b) $t^* = 98.5, \alpha = 23.0° \uparrow$

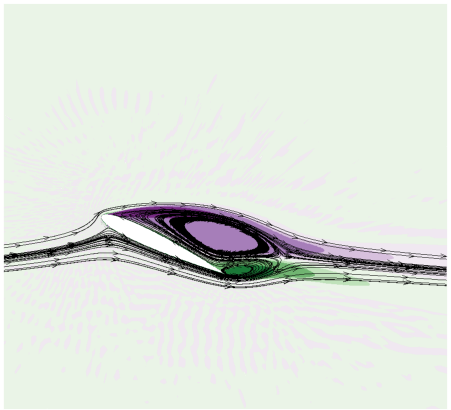

(c) $t^* = 102.4, \alpha = 25.0° \uparrow$

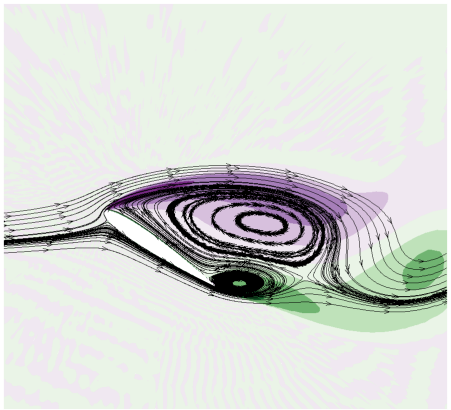

(d) $t^* = 125.9, \alpha = 33.7° \uparrow$

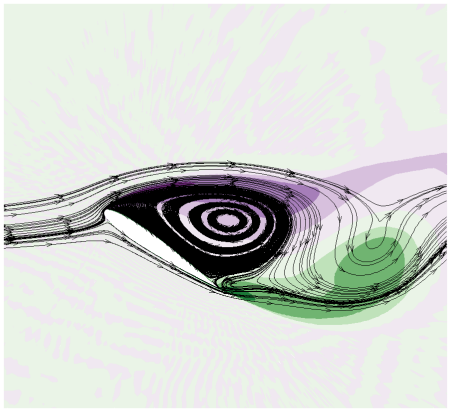

(e) $t^* = 149.5, \alpha = 34.0° \downarrow$

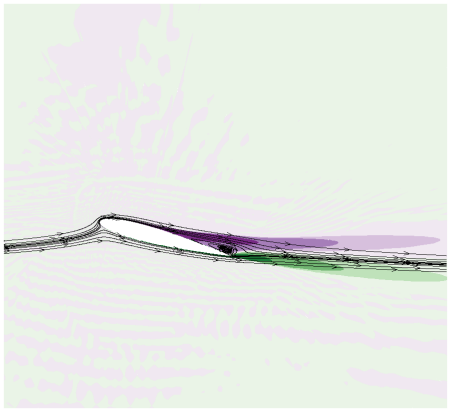

(f) $t^* = 194.1, \alpha = 14.7° \downarrow$

Fig. 14 Streamlines overlaid with vorticity contours for Case D (contour legend shown in subfigure (a)).

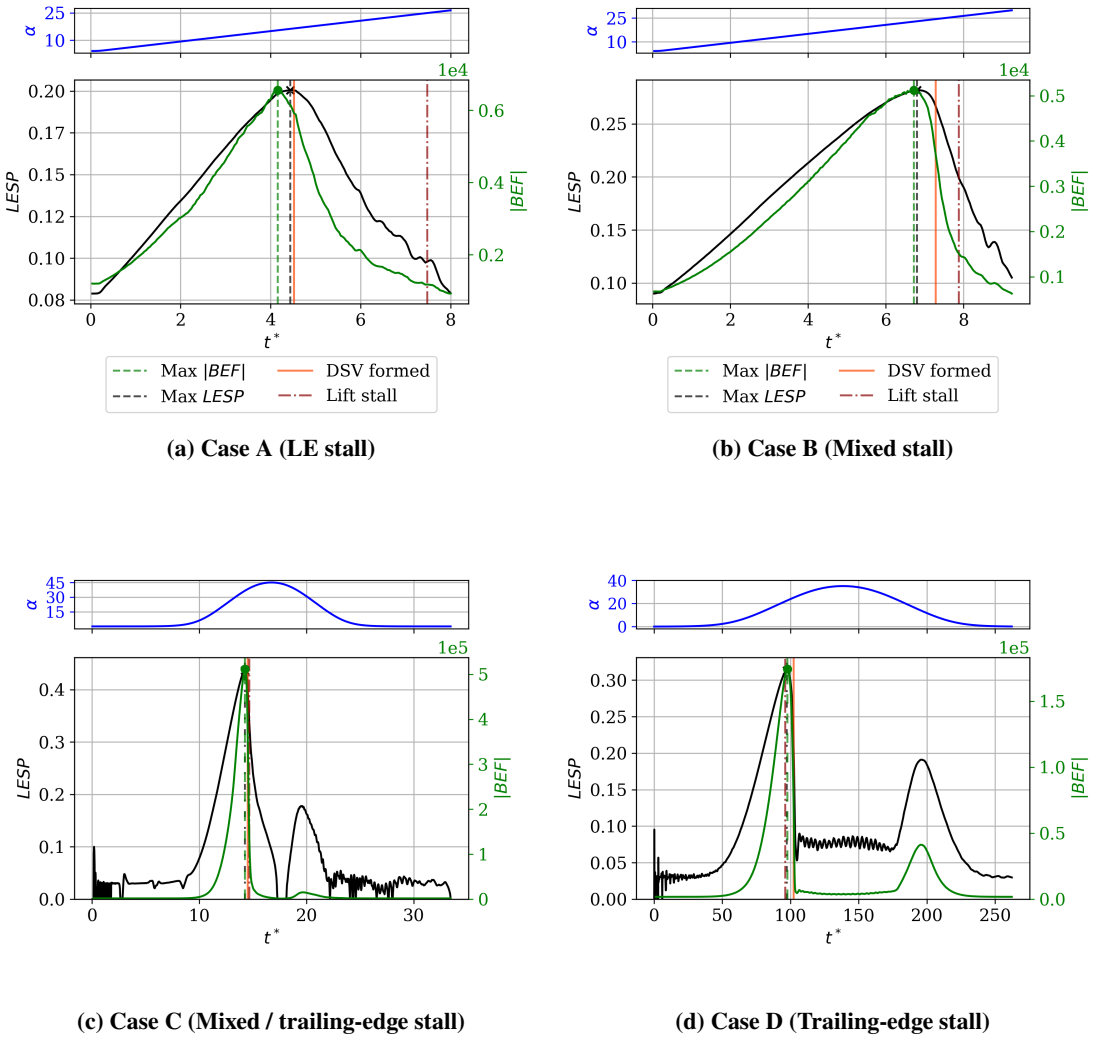

(a) Case A (LE stall)

(b) Case B (Mixed stall)

(c) Case C (Mixed / trailing-edge stall)

(d) Case D (Trailing-edge stall)

Fig. 15 Variation of $LESP$ (black) and BEF (green) for leading-edge (a), mixed (b and c) and trailing-edge (d) stalls.

trailing-edge separation in advance of DSV formation. However, for the extreme trailing-edge case considered, lift stall occurs before either criteria reaches its maximum. It has to be noted that the pitch rate for this case is very low ($K = 0.005$). Therefore, it might be worthwhile to study trailing-edge stall cases with higher pitch rates, lying between case D and case C. Nevertheless, the observed trend based on the four cases considered is a decrease in delay between the parameters reaching their maxima and the crucial point (DSV formation/lift stall), as trailing-edge separation becomes more significant.

Appendix

A. Comparison of LES and RANS results

1. Case A

Figure 16 compares the unsteady aerodynamic coefficients between LES (black, solid) and RANS (pink, dashed) for Case A. We see that the peak values of the coefficients occur slightly later for RANS. For example, lift stall (peak in c_l)

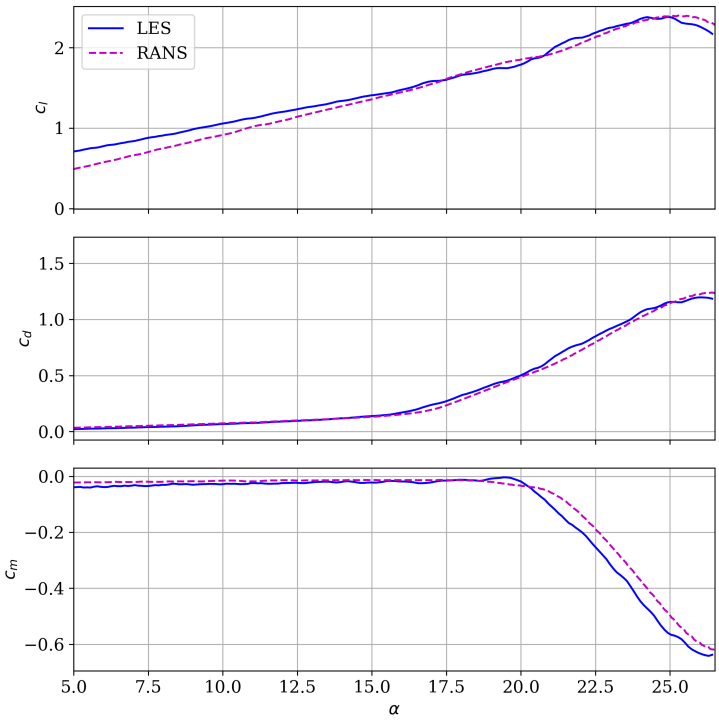

Fig. 16 Comparison of unsteady aerodynamic coefficients between LES and RANS for Case A.

is shifted by about 0.4° aft. Also, finer variations in the coefficients due to small scale structures that are generated are not captured in RANS, as expected. However, the overall match in terms of magnitudes, trends etc. is quite good.

Figure 17 compares the variation of $LESP$ and $|BEF|$ between LES and RANS. For both parameters, RANS overpredicts the maximum value, and shifts it aft in time. For $LESP$ this shift is about 0.7°, while for BEF it is closer to 1°. The maximum value is overpredicted by 4% for $LESP$ and 20% for BEF. These larger discrepancies for the BEF could be because the BEF calculation involves higher order derivatives at the wall as opposed to $LESP$, which uses C_p. Small errors in mean quantities such as C_p are amplified with higher-order derivatives. Nevertheless, RANS does capture the trend of the variation. The BEF reaches its maximum magnitude about 0.5° before the $LESP$. For our purposes, i.e. identifying the maxima of $LESP$ and BEF criteria relative to DSV formation, these slight shifts are acceptable since we expect that there is an aft shift in time for all of these events. We therefore utilize RANS for evaluating the above criteria for higher Re_c cases.

Acknowledgements

Funding for this research is provided by the National Science Foundation (Grants CBET-1554196 and 1935255). Co-author Sharma acknowledges the support provided to him by the 2019 AFOSR Summer Faculty Fellowship. Co-author Narsipur acknowledges Dr. Jack Edwards of North Carolina State University for the REACTMB-INS code used for the computations in this effort. Computational resources are provided by NSF XSEDE (Grant #TG-CTS130004) and the Argonne Leadership Computing Facility, which is a DOE Office of Science User Facility supported under Contract DE-AC02-06CH11357. We acknowledge the assistance by Drs. Miguel Visbal and Daniel Garmann from the Air Force Research Laboratory in providing initial LES solutions.

References

[1] Ramesh, K., Gopalarathnam, A., Granlund, K., Ol, M. V., and Edwards, J. R., "Discrete-vortex method with novel shedding criterion for unsteady aerofoil flows with intermittent leading-edge vortex shedding," *Journal of Fluid Mechanics*, Vol. 751, 2014, p. 500–538. https://doi.org/10.1017/jfm.2014.297.

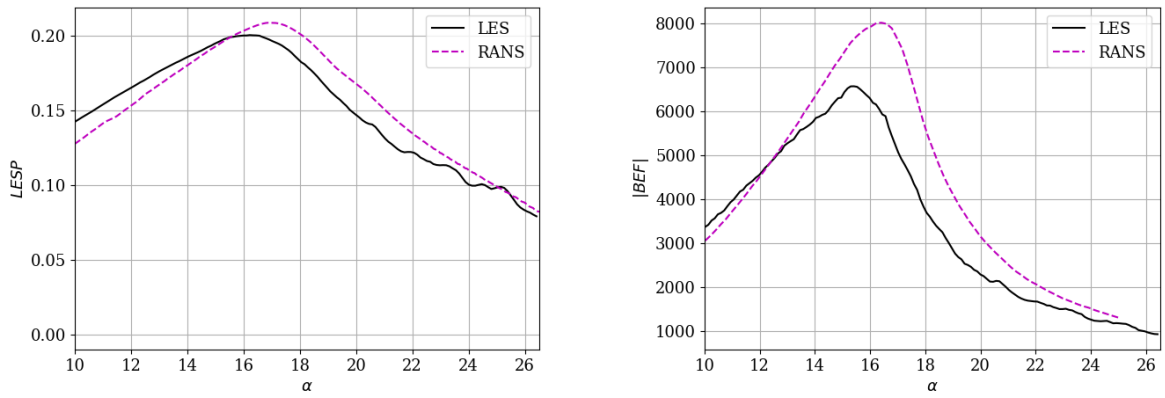

(a) $LESP$ **(b)** BEF

Fig. 17 Comparison of $LESP$ and BEF from LES and RANS for Case A.

[2] Narsipur, S., Hosangadi, P., Gopalarathnam, A., and Edwards, J. R., "Variation of leading-edge suction during stall for unsteady aerofoil motions," *Journal of Fluid Mechanics*, Vol. 900, 2020, p. A25. https://doi.org/10.1017/jfm.2020.467.

[3] Sudharsan, S., Ganapathysubramanian, B., and Sharma, A., "A vorticity-based criterion to characterise leading-edge dynamic stall onset," *Journal of Fluid Mechanics*, 2021. (accepted).

[4] McCroskey, W. J., "The phenomenon of dynamic stall," Tech. rep., NASA, Washington, DC, 1981.

[5] Müller-Vahl, H. F., Nayeri, C. N., Paschereit, C. O., and Greenblatt, D., "Dynamic stall control via adaptive blowing," *Renewable Energy*, Vol. 97, 2016, pp. 47–64. https://doi.org/https://doi.org/10.1016/j.renene.2016.05.053, URL https://www.sciencedirect.com/science/article/pii/S0960148116304633.

[6] Santra, S., and Greenblatt, D., "Dynamic Stall Control Model for Pitching Airfoils with Slot Blowing," *AIAA Journal*, Vol. 59, No. 1, 2021, pp. 400–404. https://doi.org/10.2514/1.J059818, URL https://doi.org/10.2514/1.J059818.

[7] Lombardi, A. J., Bowles, P. O., and Corke, T. C., "Closed-Loop Dynamic Stall Control Using a Plasma Actuator," *AIAA Journal*, Vol. 51, No. 5, 2013, pp. 1130–1141. https://doi.org/10.2514/1.J051988, URL https://doi.org/10.2514/1.J051988.

[8] Yu, H., and Zheng, J., "Numerical investigation of control of dynamic stall over a NACA0015 airfoil using dielectric barrier discharge plasma actuators," *Physics of Fluids*, Vol. 32, No. 3, 2020, p. 035103. https://doi.org/10.1063/1.5142465, URL https://doi.org/10.1063/1.5142465.

[9] Rice, T. T., Taylor, K., and Amitay, M., "Pulse modulation of synthetic jet actuators for control of separation," *Phys. Rev. Fluids*, Vol. 6, 2021, p. 093902. https://doi.org/10.1103/PhysRevFluids.6.093902, URL https://link.aps.org/doi/10.1103/PhysRevFluids.6.093902.

[10] Chandrasekhara, M. S., "Compressible dynamic stall vorticity flux control using a dynamic camber airfoil," *Sadhana*, Vol. 32, 2007, pp. 93–102. https://doi.org/10.1007/s12046-007-0008-8, URL https://doi.org/10.1007/s12046-007-0008-8.

[11] Leishman, J. G., and Beddoes, T. S., "A Semi-Empirical Model for Dynamic Stall," *J. Am. Helicopter Soc.*, Vol. 34, 1989, pp. 3–17.

[12] Deparday, J., and Mulleners, K., "Critical evolution of leading edge suction during dynamic stall," *Journal of Physics: Conference Series*, Vol. 1037, No. 2, 2018. https://doi.org/10.1088/1742-6596/1037/2/022017.

[13] Deparday, J., and Mulleners, K., "Modeling the interplay between the shear layer and leading edge suction during dynamic stall," *Physics of Fluids*, Vol. 31, No. 10, 2019, p. 107104. https://doi.org/10.1063/1.5121312.

[14] Corke, T. C., and Thomas, F. O., "Dynamic Stall in Pitching Airfoils: Aerodynamic Damping and Compressibility Effects," *Annual Review of Fluid Mechanics*, Vol. 47, No. 1, 2015, pp. 479–505. https://doi.org/10.1146/annurev-fluid-010814-013632, URL http://www.annualreviews.org/doi/10.1146/annurev-fluid-010814-013632.

[15] Mccroskey, W. J., Mcalister, K. W., Carr, L. W., Pucci, S. L., Lambert, O., and Indergrand, R. F., "Dynamic Stall on Advanced Airfoil Sections," *Journal of The American Helicopter Society*, Vol. 26, 1981, pp. 40–50.

[16] Sharma, A., and Visbal, M., "Numerical investigation of the effect of airfoil thickness on onset of dynamic stall," *Journal of Fluid Mechanics*, Vol. 870, 2019, p. 870–900. https://doi.org/10.1017/jfm.2019.235.

[17] Visbal, M. R., and Gaitonde, D. V., "On the Use of Higher-Order Finite-Difference Schemes on Curvilinear and Deforming Meshes," *Journal of Computational Physics*, Vol. 181, No. 1, 2002, pp. 155–185.

[18] Cassidy, D. A., Edwards, J. R., and Tian, M., "An Investigation of Interface-Sharpening Schemes for Multiphase Mixture Flows," *Journal of Computational Physics*, Vol. 228, No. 16, 2009, pp. 5628–5649.

[19] Spalart, P. R., and Allmaras, S. R., "A One-Equation Turbulence Model for Aerodynamic Flows," AIAA Paper 92–0439, 1992.

[20] Edwards, J. R., and Chandra, S., "Comparison of Eddy Viscosity - Transport Turbulence Models for Three-Dimensional, Shock-Separated Flowfields," *AIAA Journal*, Vol. 34, No. 4, 1996, pp. 756–763.

[21] Narsipur, S., Gopalarathnam, A., and Edwards, J. R., "Low-Order Model for Prediction of Trailing-Edge Separation in Unsteady Flow," *AIAA Journal*, Vol. 57, No. 1, 2019, pp. 191–207.

[22] Narsipur, S., Gopalarathnam, A., and Edwards, J. R., "Low-Order Modeling of Airfoils with Massively Separated Flow and Leading-Edge Vortex Shedding," Proceedings of the AIAA Aerospace Sciences Meeting, Kissimmee, FL 2018-0813, January 2018.

[23] Ramesh, K., Gopalarathnam, A., Edwards, J. R., Ol, M. V., and Granlund, K., "An unsteady airfoil theory applied to pitching motions validated against experiment and computation," *Theoretical and Computational Fluid Dynamics*, Vol. 27, 2013, p. 843–864. https://doi.org/10.1007/s00162-012-0292-8, URL https://doi.org/10.1007/s00162-012-0292-8.

[24] Mccullough, G. B., and Gault, D. E., "Examples of three representative types of airfoil-section stall at low speed," Tech. rep., 1951.

[25] O'Meara, M. M., and Mueller, T. J., "Laminar separation bubble characteristics on an airfoil at low Reynolds numbers," *AIAA Journal*, Vol. 25, No. 8, 1987, pp. 1033–1041. https://doi.org/10.2514/3.9739, URL https://doi.org/10.2514/3.9739.

[26] Doligalski, T., "Vortex Interactions with Walls," *Annual Review of Fluid Mechanics*, Vol. 26, No. 1, 1994, pp. 573–616. https://doi.org/10.1146/annurev.fluid.26.1.573.